



HAL
open science

Urban flood modeling with porous shallow-water equations: a case study of model errors in the presence of anisotropic porosity

Byunghyun Kim, Brett F. Sanders, James Famiglietti, Vincent Guinot

► **To cite this version:**

Byunghyun Kim, Brett F. Sanders, James Famiglietti, Vincent Guinot. Urban flood modeling with porous shallow-water equations: a case study of model errors in the presence of anisotropic porosity. *Journal of Environmental Hydrology*, 2015, 523, pp.680-692. 10.1016/j.jhydrol.2015.01.059 . hal-01118743

HAL Id: hal-01118743

<https://hal.science/hal-01118743>

Submitted on 19 Feb 2015

HAL is a multi-disciplinary open access archive for the deposit and dissemination of scientific research documents, whether they are published or not. The documents may come from teaching and research institutions in France or abroad, or from public or private research centers.

L'archive ouverte pluridisciplinaire **HAL**, est destinée au dépôt et à la diffusion de documents scientifiques de niveau recherche, publiés ou non, émanant des établissements d'enseignement et de recherche français ou étrangers, des laboratoires publics ou privés.

Urban flood modeling with porous shallow-water equations: a case study of model errors in the presence of anisotropic porosity

Byunghyun Kim^{1,2}, Brett F. Sanders^{1,2,*}, James S. Famiglietti^{1,2,4}, Vincent Guinot⁵

Abstract

Porous shallow-water models (porosity models) simulate urban flood flows orders of magnitude faster than classical shallow-water models due to a relatively coarse grid and large time step, enabling flood hazard mapping over far greater spatial extents than is possible with classical shallow-water models. Here the errors of both isotropic and anisotropic porosity models are examined in the presence of anisotropic porosity, i.e., unevenly spaced obstacles in the cross-flow and along-flow directions, which is common in practical applications. We show that porosity models are affected by three types of errors: (a) structural model error associated with limitations of the shallow-water equations, (b) scale errors associated with use of a relatively coarse

*Tel: +1 949 824 4327; fax +1 949 824 3672

Email address: bsanders@uci.edu (Brett F. Sanders)

URL: <http://sanders.eng.uci.edu> (Brett F. Sanders)

¹UC Center for Hydrologic Modeling, Irvine, CA, USA

²Department of Civil and Environmental Engineering, University of California, Irvine, CA, 92697, USA

³Department of Earth System Science, University of California, Irvine, CA, 92697, USA

⁴NASA Jet Propulsion Laboratory, California Institute of Technology, Pasadena, CA, 91109, USA

⁵Université Montpellier 2, HydroSciences Montpellier, CC MSE, Place Eugène Bataillon, 34095 Montpellier Cedex 5, France

grid, and (c) porosity model errors associated with the formulation of the porosity equations to account for sub-grid scale obstructions. Results show that porosity model errors are generally larger than scale errors but smaller than structural model errors, and that porosity model errors in both depth and velocity are substantially smaller for anisotropic versus isotropic porosity models. Results also show that the anisotropic porosity model is equally accurate as classical shallow-water models when compared directly to gage measurements, while the isotropic model is less accurate. The anisotropic porosity model is also able to resolve flow variability at smaller spatial scales than the isotropic model because the latter is restricted by the assumption of a representative elemental volume (REV) which is considerably larger than the size of obstructions. Finally, results show that substantial differences in flow attributes may exist between the point-scale and the porosity model grid scale, as a result of unresolved wakes and wave reflections from flow obstructions.

Keywords: Porous shallow water equations, Finite volume model, Anisotropic porosity, Dam-break flood, Urban flood.

1. Introduction

Urban flood modeling is now possible at centimetric resolution or better with modern laser scanning data and flood models (Bates, 2012; Sampson et al, 2012), but it is not advisable at this resolution over entire floodplains as the computational costs and memory demands are forbidding except on massively parallel computing architectures. Commonly used models are constrained by the Courant, Friedrichs, Lewy (CFL) condition for both stability

1 and accuracy which dictates nearly an order-of-magnitude increase in com-
 2 putational effort every time the mesh resolution is doubled. For a Cartesian
 3 grid with a cell size of Δx , the computational cost C of integrating a flood
 4 over a specified duration will scale as the product of the required number of
 5 computational cells n_c and time steps n_t ,

$$C \sim n_c n_t \sim \frac{1}{\Delta x^3} \quad (1)$$

6 because $n_c \sim \Delta x^{-2}$ and the CFL requirement to scale Δt with Δx . Thus,
 7 halving the cell size causes an eight fold increase in computational effort
 8 (nearly an order of magnitude) and at least a four-fold increase in memory
 9 demands. Previous work has shown that porosity models reduce computa-
 10 tional demands by orders of magnitude (Yu and Lane, 2005; McMillan and
 11 Brasington, 2007; Soares-Frazão et al., 2008; Sanders et al., 2008).

12 Porous shallow-water equations (porosity models) resolve urban flood-
 13 ing at a relatively coarse (and efficient) resolution compared to available
 14 geospatial data using additional parameters that account for sub-grid scale
 15 topographic features affecting the movement and storage flood water (De-
 16 fina, 2000; Yu and Lane, 2005; McMillan and Brasington, 2007; Sanders et
 17 al., 2008; Soares-Frazão et al., 2008; Cea and Vázquez-Cendón, 2010; Chen
 18 et al., 2012; Guinot, 2012; Schubert and Sanders, 2012). In practice, the idea
 19 is to use a cell size on the order of meters or dekameters instead of a sub-
 20 metric resolution. This gives rise to models that resolve flooding at the *pore*
 21 *scale* roughly corresponding to the width of roadways and open spaces be-
 22 tween buildings, in contrast with classical shallow-water models that resolve
 23 flooding at the *point scale*, as approximated by the grid resolution.

24 Sanders et al. (2008) and Guinot (2012) introduce two alternative formu-

1 lations of porosity models to capture porosity anisotropy, which can be ex-
2 pected in most practical applications. Anisotropy occurs in urban landscapes
3 when there are preferential flow directions such as wide streets and narrow al-
4 leys aligned in perpendicular directions. Hypothetical examples of anisotropic
5 flow have been presented in previous studies (Sanders et al., 2008; Guinot,
6 2012), including numerous cases with angled channel-like flows through urban
7 areas. Additionally, Schubert and Sanders (2012) present a field-scale appli-
8 cation of an anisotropic porosity model that outperforms models based on
9 the classical shallow-water equations.

10 Porosity heterogeneity exists when the size of flow paths is spatially vari-
11 able, and different porosity models resolve heterogeneity over different scales.
12 Isotropic porosity models are restricted to scales larger than the length scale
13 of the Representative Elemental Volume (REV). This is typically an order
14 of magnitude larger than the scale of flow obstructions in urban flood appli-
15 cations, nominally a kilometer or more (Guinot, 2012). On the other hand,
16 the anisotropic porosity model developed by Sanders et al. (2008) does not
17 require the existence of an REV and can resolve heterogeneity at the grid
18 scale.

19 Since porosity anisotropy is a critical consideration for practical applica-
20 tions, this study presents modeling of a unique experimental test case involv-
21 ing dam-break flow through an anisotropic array of obstructions, which builds
22 on earlier experimental work and modeling studies focused on isotropic ar-
23 rays of obstructions (Testa et al., 2007; Soares-Frazão and Zech, 2008). A
24 classical shallow-water model and both isotropic and anisotropic porosity
25 models are applied and calibrated. The objective is to measure and report

1 the magnitude of porosity model errors in an absolute sense and also relative
2 to other errors which collectively limit the overall accuracy of the model. A
3 better understanding of errors is needed to effectively use porosity models
4 in flood hazard mapping. Three types of errors are reported: (a) structural
5 model errors associated with the shallow-water equations which constitute
6 the foundation of the porosity models, (b) scale errors arising from a grid
7 size that matches the pore scale instead of the point scale, and (c) porosity
8 model errors associated the parameterization of sub-grid scale obstructions.
9 Results point to significant differences in porosity model errors across alter-
10 native porosity model formulatoins.

11 **2. Methods and Materials**

12 *2.1. Porosity Definition*

13 Porosity can be defined in more than one way, namely as a volume average
14 fraction of pore space in a porous media or as an areal average fraction of
15 pore space, as in a slice through the porous medium (Bear, 1988). Both
16 volumetric and areal porosity can be expected to vary spatially in the case
17 of a heterogeneous porous medium, and areal porosity can also vary with
18 the orientation of the plane over which the areal average is taken, and thus
19 exhibit anisotropy. If an urban land surface filled with solid features is taken
20 as a porous medium, then the pore space represents the gaps between the
21 solid features, the volumetric porosity represents the fraction of the land
22 surface able to store water, and the areal porosity represents the fraction of
23 space available for flood conveyance which is directionally dependent.

1 *2.2. Porous Shallow-Water Equations*

2 The anisotropic porosity model of Sanders et al. (2008) is written as integral
 3 statements of mass and momentum conservation for an arbitrary 2D domain
 4 Ω with boundary Γ and unit outward normal vector \mathbf{n} as follows,

$$\frac{\partial}{\partial t} \int_{\Omega} i \mathbf{U} d\Omega + \oint_{\Gamma} i \mathbf{E} \cdot \mathbf{n} d\Gamma = \oint_{\Gamma} i \mathbf{H} \cdot \mathbf{n} d\Gamma + \int_{\Omega} i \mathbf{S} d\Omega \quad (2)$$

5 where

$$\mathbf{U} = \begin{pmatrix} h \\ uh \\ vh \end{pmatrix} \quad \mathbf{E} = \begin{pmatrix} uh & vh \\ u^2h + \frac{1}{2}gh^2 & uvh \\ uvh & v^2h + \frac{1}{2}gh^2 \end{pmatrix} \quad (3)$$

$$\mathbf{S} = \begin{pmatrix} 0 \\ -(c_D^f + c_D^b)uV \\ -(c_D^f + c_D^b)vV \end{pmatrix} \quad \mathbf{H} = \begin{pmatrix} 0 & 0 \\ \frac{1}{2}gh|_{\eta_o}^2 & 0 \\ 0 & \frac{1}{2}gh|_{\eta_o}^2 \end{pmatrix} \quad (4)$$

7 where $u=x$ -component of velocity, $v=y$ -component of velocity, g =gravitational
 8 constant, $V = (u^2 + v^2)^{1/2}$, c_D^f is a ground friction drag coefficient, c_D^b is a
 9 drag coefficient for sub-grid scale flow obstructions, and $h|_{\eta_o}$ is the depth cor-
 10 responding to a piecewise constant water surface elevation η_o and piecewise
 11 linear ground elevation z within Ω . The \mathbf{H} term is introduced to transform
 12 the classical ground slope source term to a boundary integral that preserves
 13 stationary solutions. Based on the limits of this transformation, the momen-
 14 tum equations appearing in Eq. 2 are restricted to numerical schemes that
 15 are first- or second order accurate in space (Sanders et al., 2008).

16 The variable $i(x, y)$ appearing in Eq. 2 is defined for the spatial domain
 17 $D \in \mathbf{R}^2$ and represents a binary density function that takes on a value of
 18 zero or unity depending on the presence or absence of a solid flow barrier as
 19 follows (Sanders et al., 2008),

$$i(x, y) = \begin{cases} 0 & \text{if } (x, y) \in D_b \\ 1 & \text{otherwise} \end{cases} \quad (5)$$

1 where D_b is a subdomain of D that corresponds to solid obstacles. Two grid-
 2 based porosity parameters are dependent on the density function (Eq. 5) as
 3 follows,

$$\phi_j = \frac{1}{\Omega_j} \int_{\Omega_j} i \, d\Omega \quad \psi_k = \frac{1}{\Gamma_k} \int_{\Gamma_k} i \, d\Gamma \quad (6)$$

4 where Ω_j corresponds to the two-dimensional (2D) spatial domain of the j^{th}
 5 computational cell and Γ_k corresponds to the k^{th} computational edge of a
 6 mesh. Note that ϕ_j represents the fraction of a cell area occupied by voids,
 7 and ψ_k represents the fraction of a cell edge occupied by voids. Consequently,
 8 these parameters affect the relative storage of cells and conveyance between
 9 cells, respectively. Importantly, anisotropic blockage effects are explicitly
 10 resolved by the distribution of ψ_k values across the computational mesh. It
 11 is noted that isotropic porous shallow-water equations can be recovered from
 12 Eq. 2 under the assumption that $\phi_j = \psi_k \forall k$. Additionally, Eq. 2 revert to the
 13 classical shallow-water equations in the limit that $i(x, y) = 1$.

14 Presently it is not clear how well isotropic and anisotropic porosity mod-
 15 els resolve flow at the pore scale where information is needed to assess the
 16 risks facing individual land parcels in an urban area, especially when the
 17 obstructions exhibit anisotropy. Eqs. 2 resolve flow properties on a grid-cell
 18 by grid-cell basis which corresponds to the pore scale since the model re-
 19 quires a grid that aligns cells with pore spaces (Sanders et al., 2008). In
 20 contrast, isotropic models require the existence of an REV where the poros-
 21 ity is scale-independent and where areal and volumetric porosities converge
 22 to a single scalar value (Bear, 1988). The length scale of the REV is roughly

1 an order of magnitude larger than the length scale of obstructions in urban
2 landscapes (Guinot, 2012), so assuming that pore sizes and obstructions are
3 similarly sized, the isotropic models theoretically resolve flow at roughly an
4 order of magnitude larger scale than the anisotropic model presented here.
5 On the other hand, Guinot (2012) suggests that isotropic models can yield
6 representative results at scales 2-3 times smaller than the REV scale.

7 The ground friction drag coefficient is parameterized by a Darcy-Weisbach
8 f as follows, $c_D^f = f/8$ which is in turn computed using a modified form
9 of the Haaland equation (Haaland, 1983) presented by Arega and Sanders
10 (2004) which considers the Nikuradse sand-grain roughness height k_s and
11 the depth-based Reynolds number $Re_h = Vh/\nu$, where ν represents the
12 kinematic viscosity. The building drag coefficient is scaled by the projected
13 area of solid barriers as follows, $c_D^b = \frac{1}{2}c_D^o a_f h$ where a_f represents frontal
14 area (Nepf, 1999). The units of a_f are length^{-1} , corresponding to the frontal
15 width of obstructions in Ω normalized by Ω . c_D^o is classical drag coefficient
16 that accounts for shape and Reynolds number effects on drag (Sanders et al.,
17 2008).

18 *2.3. Numerical Methods*

19 The integral porosity model is solved using a Godunov-based finite vol-
20 ume scheme that allows for triangular, quadrilateral, or mixed meshes (Kim
21 et al., 2014). The scheme uses Roe's approximate Riemann solver with a
22 critical flow fix, an adaptive method of variable reconstruction for uneven
23 topography that minimizes numerical dissipation (Begnudelli et al., 2008), a
24 local time stepping scheme (Sanders, 2008), a improved Volume-Free Surface-
25 Reconstruction (VFR) technique for wetting and drying, and inclusion of grid

1 based porosity parameters (Sanders et al., 2008) which is of particular inter-
2 est here. The scheme is explicit and conditionally stable in accordance with
3 a CFL condition (Kim et al., 2014).

4 *2.4. Laboratory Experiment*

5 Laboratory-scale modeling of anisotropic blockage effects was carried out
6 in a physical model constructed at the Korea Institute of Construction Tech-
7 nology (KICT). Fig. 1(a) and (b) show the plan view and side view of the
8 physical model, respectively, and Fig. 1(c) shows the location of gage stations
9 and blocks. The experimental tank is 30x30 m and includes a reservoir, a
10 dam, and a floodplain. The width and length of the reservoir are 5 m and
11 30 m, respectively, and the width and length of the floodplain are 28 m and
12 24 m, respectively (Yoon, 2007).

13 The reservoir and floodplain surfaces are horizontal and treated with mor-
14 tar to achieve a uniform roughness. The floodplain is vertically offset 0.4 m
15 above the reservoir, and the two areas are separated by a concrete wall with
16 a sliding gate that is opened horizontally and symmetrically to simulate a
17 breach. The gate moves along a rail set equal in height to the floodplain.
18 To initiate a flood, the sliding gate opens at a velocity of 0.18 m/s until
19 the breach reaches a maximum width of 1.0 m. At the outer boundary of
20 the model floodplain, there is a vertical drop of 0.4 m into a channel 1.0 m
21 wide for drainage. The floodplain and perimeter drainage channel were de-
22 signed to ensure a free-outflow condition along the entire perimeter. The
23 solid blocks are 0.2x0.2 m square pillars made of an acrylic shell and filled
24 with concrete for stability during flood conditions. The blocks were arranged
25 as two 3x3 groups that are symmetrically aligned about the centerline of the

1 dam as shown in Fig. 1 (Yoon, 2007).

2 A total of 17 capacitance-type gages (Model CHT4-60, KENEK, Tokyo,
3 Japan) were installed to measure transient flow depths as shown in Fig. 1(c).
4 The probes measured depths in the range 0 to 30 cm and sampled at a
5 rate of 5 Hz (0.2 sec sampling interval). It is noted that several stations
6 are positioned as symmetric pairs about the dam centerline as shown in
7 Fig. 1(c). Two different flow scenarios are considered corresponding to an
8 initial reservoir water depth (h_0) of 0.30 m and 0.45 m, measured relative to
9 the floodplain elevation (Yoon, 2007).

10 Within each 3x3 cluster, the gap between buildings is 0.1 m facing the
11 dam (section E-E' in Fig. 1(d)) and 0.4 m perpendicular to the dam (sec-
12 tion G-G' in Fig. 1(d)). This introduces a strong degree of anisotropy in
13 the porosity field, a 1 to 4 ratio in the cross-sectional area available for flow
14 between blocks. The KICT problem also introduces pore scale heterogeneity
15 in the porosity distribution. For example, considering again Fig. 1(d), the
16 areal porosity ψ varies significantly between Sections D-D' and E-E' in the y
17 direction, with $\psi_E < \psi_D$, and between Sections G-G' and F-F' in the x direc-
18 tion, with $\psi_G < \psi_F$. Similarly, the volumetric porosity ϕ varies significantly
19 between domain a and b shown in Fig. 1(d), with $\phi_b < \phi_a$.

20 2.5. Summary of Models

21 A classical shallow-water model (CSW), the anisotropic porosity model
22 (PSW-A), and four isotropic porosity models (PSW-I) were applied. Addi-
23 tionally, results of the classical shallow-water model were averaged over each
24 porosity-model grid cell to yield a pore scale classical shallow-water model
25 result (CSW-P). Table 1 presents a summary of the seven models, and Fig. 2

1 presents the computational meshes used. Note that Fig. 2b corresponds to
 2 the gap-conforming mesh required of the anisotropic model (Sanders et al.,
 3 2008), where vertices are placed at the centroid of obstructions, cells are
 4 aligned with pore spaces, and edges intersect constrictions in the pore space.
 5 Additionally, Fig. 2c corresponds to a region conforming mesh that precisely
 6 circumscribes the subdomain filled with flow barriers (Soares-Frazão et al.,
 7 2008; Guinot, 2012). Four variants of the isotropic porosity model are used
 8 to account for both mesh designs and two alternative porosity values cor-
 9 responding to the region-average volumetric porosity Soares-Frazão et al.
 10 (2008) and the areal porosity (Guinot, 2012), as shown in Table 1. It is
 11 noted that an REV cannot be rigorously established in this test case due to
 12 the anisotropy, heterogeneity and limited spatial extent of the flow barriers,
 13 so the assumptions required to apply the isotropic model are not satisfied.
 14 However, isotropic models have yielded credible predictions in other applica-
 15 tions where these requirements were not satisfied (Guinot, 2012), motivating
 16 further study here.

17 *2.6. Definition of Errors*

18 Three types of errors are reported: (a) structural model errors, (b) scale
 19 errors and (c) porosity model errors. Structural model errors are defined
 20 by the difference, as measured by $L_1 = \sum_{j=1}^N |(w_1)_j - (w_2)_j|/N$, between the
 21 converged CSW prediction and gage measurements of flood depths. Scale er-
 22 rors are defined by the difference between the CSW (point scale) and CSW-P
 23 (pore scale) predictions at gage locations, and are computed for both depth
 24 and velocity. Porosity model errors are defined by the difference between
 25 porosity model predictions and CSW-P at gage locations (pore scale com-

1 parison), and are evaluated for both depth and velocity.

2 *2.7. Model Parameterization and Calibration*

3 In all seven models, mesh vertex heights were assigned based on reservoir
4 or floodplain bed elevations, and mesh cells were assigned a Nikuradse sand-
5 grain roughness height k_s to model bottom shear. Further, a no-normal-flux
6 boundary condition was enforced along the reservoir boundaries and concrete
7 wall separating the reservoir and floodplain, and a free-outflow boundary
8 condition was enforced along the remaining three sides of the floodplain.
9 The gate opening was modeled as an instantaneous breach since the time
10 scale of opening (<3 s) is short compared with the time-scale of the breach
11 flow (>100 s).

12 To apply the anisotropic porosity model, the cell-based porosity ϕ_j and
13 edge-based porosity ψ_k were computed based on the intersection of the mesh
14 with the footprint of the solid blocks following previously described methods
15 (Sanders et al., 2008; Schubert and Sanders, 2012). Additionally, the frontal
16 area parameter a_f required to parameterize drag was computed on a cell-by-
17 cell basis in accordance with the projected area facing the dam as described
18 previously (Sanders et al., 2008).

19 To apply the isotropic porosity models, ϕ_j and ψ_k were assigned a uniform
20 value inside the block zone as shown in Table 1. Volumetric porosity values
21 used in PSW-I-1A and PSW-I-2A are based on the spatial extent of cells
22 that contact the obstructions, and the porosity values differ slightly based
23 on the mesh. Areal porosity values used in PSW-I-1B and PSW-I-2B are
24 based on the transect E-E' in Fig. 1d. A uniform frontal area parameter was
25 also specified inside the block zone equal to the total frontal area facing the

1 dam, normalized by the size of the block zone. This corresponds to 0.83 and
2 1.29 m^{-1} (Table 1) for the meshes shown Fig. 2b and 2c, respectively.

3 Outside the block zone, a porosity value of unity was assigned in all
4 porosity models. Also, the frontal area was set to zero.

5 The roughness parameter, k_s , was manually calibrated by applying CSW
6 to the first KICT flow scenario ($h_0=0.30 \text{ m}$) with k_s values ranging from 0.03
7 to 0.3 cm, which is an established range for concrete (Munson et al., 2006).
8 The k_s value achieving the best agreement between predicted depths and
9 gage measurements (minimum L_1 norm) was subsequently used in all other
10 models and in the second KICT flow scenario ($h_0=0.45 \text{ m}$).

11 To calibrate c_D^o , each of the porosity models was applied to the first KICT
12 flow scenario with c_D^o values ranging from 1.0 to 3.0. This range corresponds
13 to rectangular shaped blocks in an idealized two-dimensional flow (Munson
14 et al., 2006), and it is recognized that c_D^o may also vary depending on shel-
15 tering effects from the clustering of solid barriers and three-dimensional flow
16 effects (Sanders et al., 2008). Several options deserve consideration as the
17 reference solution for the L_1 error norm. Calibration to gage measurements
18 is the first option and is motivated by the goal of minimizing the overall
19 error in the porosity model prediction, whereas another option is calibration
20 to CSW-P predictions which is motivated by the goal of minimizing porosity
21 model errors. Further, calibration to CSW-P depth and/or velocity predic-
22 tions is possible. Here, all three options are pursued: calibration to depth
23 measurements, CSW-P predictions of depth at gage locations, and CSW-P
24 predictions of velocity at gage locations.

1 **3. Results**

2 *3.1. Convergence of the CSW model*

3 A resolution of 0.05 m was selected for CSW after a convergence check
4 with a 0.025 m mesh of approximately 1.3 million computational cells. This
5 showed that the average convergence error (measured over the simulation
6 period at each gage) of the CSW depth prediction was less than 2 mm at
7 all stations except Gage 2, where the convergence error was found to be
8 6 mm. Over all stations, the average convergence error was approximately
9 1 mm. Gage 2 is located in front of the leading row of obstructions (see
10 Fig. 1). Here, super-critical flow through the breach strikes the first row
11 of blocks, and a bow shock (hydraulic jump) forms across the width of the
12 blocks as shown in Fig. 3. Based on the curvature of the shock wave, Gage
13 2 is on the windward side of the shock and Gages 11 and 18 are on the
14 leeward side. Further, the width of the shock wave (measured in y direction
15 on Fig. 3) is minimal at Gage 2: over a distance of 30 cm in the y direction,
16 the water depth rises up from 5 cm to 16 cm, and then down again to 10 cm,
17 approximately, based on results shown in Fig. 3(b). As the mesh is coarsened
18 from 0.025 to 0.05 m resolution, this narrow band of super-elevated water is
19 diffused slightly and its windward edge moves closer to Gage 2, leading to
20 higher water depth predictions. Hence, the relatively large convergence error
21 at Gage 2 is explained by its position at the leading edge of a shock wave.
22 It is noted that porosity models use a 30 cm mesh resolution (Fig. 2(c) and
23 (d), and Table 1), which is too coarse to sharply resolve the narrow band of
24 super-elevated water at Gage 2. This shows that pore scale and point scale
25 values of flood predictions may differ substantially as a result of localized

1 wakes and wave reflections from flow obstructions.

2 3.2. Calibration of k_s

3 Fig. 4 shows CSW model predictions of depth using k_s values from 0.03 to
4 0.3 cm, compared with measurements for a selection of gages. Additionally,
5 Table 2 shows L_1 norms for CSW model. These results demonstrate that the
6 influence of roughness depends on the gage location, but overall roughness
7 does not exhibit a strong influence on the average error. The implication
8 is that momentum losses are dominated by the geometric constriction and
9 form drag associated with the solid blocks, not skin friction from the bottom
10 boundary. All subsequent modeling uses $k_s=0.03$ cm since this leads to the
11 most accurate prediction based on the values considered.

12 3.3. Calibration of c_D^o

13 Table 3 presents L_1 norms in porosity model predictions as a function
14 of c_D^o and different reference solutions. This shows that optimal c_D^o depends
15 on the porosity model and also depends on whether the goal is to minimize
16 total errors or porosity model errors. In four of the five models, minimizing
17 porosity model errors calls for a drag coefficient on the low end of the range
18 (1.0) while minimizing total errors calls for a drag coefficient at the high end
19 of the range (3.0). We conjecture that the goal of a porosity model should
20 be to reproduce as accurately as possible the pore-scale averaged solution of
21 the shallow-water equations, and not necessary match measurements. How-
22 ever, the results here clearly indicate that c_D^o can be tuned to improve the
23 agreement with measurements.

1 The calibration also shows that over a range of physically realistic drag
2 coefficient values, the anisotropic model consistently produces smaller total
3 errors and porosity model errors in flood depths. Further, the anisotropic
4 model performs particularly well with respect to velocity predictions, as the
5 porosity model errors are nearly twice as large for isotropic models versus
6 the anisotropic model.

7 In the analysis of model errors which follows, results of all three cali-
8 brations are considered and referenced as Calib1 (measured depth), Calib2
9 (CSW-P depth prediction), and Calib3 (CSW-P velocity prediction).

10 *3.4. Model Predictions and Errors*

11 Table 4 provides a summary of all model configurations and run times,
12 including optional parameter values corresponding to different calibrations.
13 Models were executed using a 3.07 GHz Intel[®] Core[™] i7 CPU with 8GB
14 RAM. The differences in run time are striking as in previous studies. Com-
15 pared with CSW, the porosity models execute almost three orders of magni-
16 tude faster.

17 Figs. 5 and 6 present predictions and gage measurements of flood depth
18 for the first ($h_0=0.30$ m) and second ($h_0=0.45$ m) test cases based on Calib1,
19 and Figs. 7 and 8 present model predictions of velocity for the first and
20 second test cases based on Calib1. Results from Calib2 and 3 are not shown
21 graphically, but Table 5 shows L_1 norms according to the porosity model,
22 the calibration, and the reference solution. L_1 norms based on flood depth
23 measurements are used to measure the structural model error in the CSW
24 model and the total error in the porosity models, while L_1 norms based on
25 the CSW-P prediction are used to measure porosity model errors. The scale

1 error is measured by an L_1 norm between the CSW and CSW-P predictions.

2 *3.4.1. Structural Model Errors*

3 The CSW prediction is shown to yield a good approximation of flood
4 depths across the spatial domain (Fig. 5), with an average error of only 0.63
5 cm (Table 5), which represents just 2% of the initial depth in the reservoir.
6 The main limitations of CSW are noted at Sta. 18 where a spurious wave is
7 measured in the experiment that is not explained by the model, and at Sta.
8 5 where the model overpredicts flood depths roughly by a factor of two. In
9 a second test case involving $h_0=0.45$ m (Fig. 6), the average error is 0.89 cm
10 (Table 5) which is again just 2% of the initial depth in the reservoir. Hence,
11 after calibration of the model to the first test case, the model performs with
12 the same relative error in a second test case.

13 *3.4.2. Scale Errors*

14 Differences between point scale (CSW) predictions and pore-scale (CSW-
15 P) predictions of flood depth constitute the scale error which is at least
16 65% smaller than the structural model error according to L_1 norms shown
17 in Table 5. In particular, the scale error in depth is 0.18 cm in the first
18 test case where the structural model error is 0.63 cm. In the second test
19 case, the scale error is 0.30 cm while the structural model error is 0.89 cm.
20 Table 5 also shows that the scale error in velocity is 7.45 and 9.12 cm/s,
21 which corresponds to about 2% of the theoretical peak velocity of a dry-bed
22 dam break flood wave, $(gh_0)^{1/2}$.

23 Fig. 5 and 6 illuminate the origin of the scale error. In the first test case
24 (Fig. 5), CSW-P notably departs from CSW at Sta. 2 which is explained

1 by the shock waves shown in Fig. 3. This occurs because at the point scale,
2 the prediction corresponds to one side of the shock or the other, while at the
3 pore scale, the prediction corresponds to a spatial average around the shock.
4 Noticeable differences also occur at two other stations outside perimeter of
5 the obstructions (e.g., Sta. 17 and 18), while differences away from the
6 obstructions (Sta. 5, 6, and 7) and at stations off center from the main flow
7 path (Sta. 19 and 20) are minimal.

8 Differences between the point scale and pore-scale velocities in Fig. 7
9 and 8 are noted at Sta. 2, 15 and 16 where relatively high velocities occur
10 due to the alignment of this channel with the dam-break flood wave. Here,
11 faster velocities occur along the centerline and slower velocities occur near
12 the blocks as a result of wakes, and the monitoring stations sample the fastest
13 moving water. Relatively large scale effects are also noted at Sta. 18 and 21.

14 *3.4.3. Porosity Model Errors*

15 Attention is now focused on porosity model errors in flood depth and
16 velocity, which are measured by a comparison of porosity model predictions
17 and CSW-P. Table 5 shows that the anisotropic porosity model introduces
18 a significantly smaller error in depth and velocity than all of the isotropic
19 porosity models. For example, in the first and second test cases, isotropic
20 model errors in depth were 65-210% and 77-240% greater than the anisotropic
21 model, respectively, based on Calib2. Additionally, isotropic model errors in
22 velocity were 83-97% and 80-86% greater than the anisotropic model for the
23 first and second test cases, respectively, based on Calib3. Data in Table 5
24 also shows that the magnitude of the porosity model errors is mostly greater
25 than or equal to the scale error, but less than the structural model errors,

1 for both depth and velocity. The exception is the second test case where the
2 anisotropic porosity model errors in depth are actually smaller than the scale
3 error.

4 The total error of the porosity models relative to point-scale predictive
5 skill is also shown in Table 5, with L_1 norms based on gage depth measure-
6 ments. The total errors of the anisotropic porosity model are nearly identical
7 to CSW and CSW-P based on Calib1, while all of the isotropic models yield
8 larger total errors. Errors in the isotropic models range from 16 to 59%
9 higher than CSW errors in the first test case, and 2 to 29% higher in the
10 second test case, based on Calib1.

11 *3.5. Spatial Variability*

12 Previously shown results reveal at-a-station dynamics, but it is also worth-
13 while to examine the spatial structure of flood predictions. For the $h_0=0.30$ m
14 case, Fig. 9 shows contours of pore-scale flood depth and vectors representing
15 the pore scale velocity magnitude and direction 50 s after the dam-break as
16 depicted by: (Fig. 9a) CSW-P model, (Fig. 9b) PSW-A model, and (Fig. 9c-f)
17 the four isotropic porosity models. CSW-P model predicts a zone of elevated
18 water (region colored green, yellow and red) that approximates a triangular
19 shape, and this shape is retained fairly well by PSW-A model, but not as
20 well by the isotropic models. The isotropic models predict a more rounded
21 shape which reflects a lack of directionality. Focusing on the bow shock in
22 front of the obstructions, CSW-P model and PSW-A model predict a lat-
23 erally distorted shape, while the isotropic models predict a more rounded
24 shape, again reflecting a lack of directionality.

25 Fig. 10 shows the flood depth distribution for the $h_0=0.30$ m case at four

1 successive times along the transects through the block zone labeled B-B' in
2 Fig. 1(c), as depicted by point scale measurements, CSW, CSW-P, and the
3 porosity models. CSW, CSW-P and PSW-A model shows the formation
4 of a bow shock 1 m from the dam and immediately upstream of the first
5 block, and an adverse free surface slope upstream of the second and third
6 block from the dam. On the other hand, the isotropic porosity models fail
7 to capture this depth variability and instead predict a relatively smooth
8 variation of the flood depth through the block zone. This is a result of using
9 a uniform porosity value through the region of obstacles, and consistent with
10 the design of isotropic models to predict flow properties at the REV scale
11 which is considerably larger than the pore scale. Fig. 9 and 10 also reveal
12 insight into the sensitivity of isotropic porosity models to the porosity value.
13 Generally, with a decrease in the porosity value, the height of the bow shock
14 increases and it shifts forwards towards the dam.

15 **4. Discussion**

16 The preceding results show that porosity model errors may be signif-
17 icantly larger than scale errors which poses an opportunity for improved
18 porosity models. The margin for improvement of the anisotropic model rela-
19 tive to flood heights is small, but the potential for improvement of the veloc-
20 ity predictions is greater and motivates improved models of flow resistance,
21 possibly allowing for more spatial variability in parameters, or even funda-
22 mentally new approaches or more advanced calibration procedures. However,
23 research directed at improving porosity model formulations should be mindful
24 of structural model errors. Based on the data presented here, the anisotropic

1 model is equally accurate as the point-scale classical shallow-water model
2 relative to flood depth prediction, so further reduction in porosity model
3 errors cannot be expected to reduce total errors. Broadly, porosity models
4 cannot be expected to predict flood heights any more accurately than the
5 pore-scale average of the foundational flow model, in this case the classical
6 shallow-water equations.

7 There is critical need for urban flood inundation models that can be
8 efficiently applied over practical scales such as a city or regional flood plain,
9 and these results and previous studies (Yu and Lane, 2005; McMillan and
10 Brasington, 2007; Soares-Frazão and Zech, 2008; Sanders et al., 2008; Guinot,
11 2012) reveal great potential to address this need. But aside from accuracy,
12 another critical question to address is whether any of the porosity models can
13 be more easily parameterized and validated in practical applications. High
14 quality site data is often available for flood modeling studies but calibration
15 data is rare, so there is a need for flood models with parameters that can
16 be estimated deterministically and relied upon to make accurate predictions.
17 This further supports use of the anisotropic model presented here because
18 porosity parameters are a deterministic function of the flow obstructions
19 (Sanders et al., 2008; Schubert and Sanders, 2012), in contrast with the
20 isotropic model where it is unclear how to define a porosity given that a range
21 of values could be used corresponding to volumetric and aerial porosities
22 defined at different spatial scales. However, calibration data may still needed
23 to estimate porosity model drag parameters (e.g., Schubert and Sanders,
24 2012). In the less common scenario where high quality site data are not
25 available to guide the porosity specification, but calibration data exists, the

1 isotropic model may be preferred as the porosity value itself can be used as
2 a calibration parameter.

3 **5. Conclusions**

4 Urban flood models based on porous shallow-water equations predict
5 flood depths and velocities with three types of errors: (a) structural model er-
6 rors associated with the limitations of the 2D shallow-water equations (e.g.,
7 hydrostatic pressure, vertical uniform velocity distributions), (b) scale er-
8 rors associated with use of a relatively coarse, pore scale grid comparable to
9 the spacing between buildings, and (c) porosity model errors related to the
10 treatment of sub-grid scale obstructions. Results show that in this unique
11 test case with anisotropy in the porosity distribution as in practical appli-
12 cations, porosity model errors are mostly greater than scale errors but less
13 than structural model errors, although in one test case the porosity model
14 error of the anisotropic model was slightly less than the scale error. Results
15 also show that porosity model errors in depth and velocity are significantly
16 higher using an isotropic porosity model compared with an anisotropic model,
17 and that the anisotropic porosity model is no less accurate than a fine grid
18 shallow-water model, based on the total error. Recognizing that all porosity
19 models reduced run times by a factor of nearly a thousand compared with
20 the classical shallow-water models, the anisotropic porosity model stands out
21 as the most efficient approach for pore-scale modeling based on its low level
22 of error, among models considered here. Additionally, the anisotropic poros-
23 ity model used here is more successful at resolving pore-scale flow variability
24 than isotropic models because the latter are constrained to scales larger than

1 the REV.

2 Results show that significant differences may exist between pore-scale and
3 point-scale flood conditions in close proximity to flow obstructions, for ex-
4 ample due to wave reflections and wakes, so porosity model flood predictions
5 should be used cautiously to inform point-scale flood risk decision-making,
6 such as whether flood heights will rise above the threshold of a door along
7 a roadway. However, results validate the utility of porosity models for map-
8 ping flood heights at the pore-scale, i.e., the average flood height across a
9 roadway.

10 Further research into porosity models should be directed at reducing
11 porosity model errors in velocity, for example with improved drag param-
12 eterizations, but should be mindful of limitations posed by structural model
13 errors. Finally, the cell averaging of fine-scale classical shallow-water model
14 predictions is found to be an effective approach for gaging the merits of alter-
15 native porosity model formulations, as this enables a direct measure of the
16 porosity model error.

17 **6. Acknowledgements**

18 This work was supported by the MRPI program of the University of Califor-
19 nia Office of the President and the Infrastructure Management and Extreme
20 Events program of the National Science Foundation (CMMI-1129730). The
21 authors wish to thank K. Yoon and his research team for their efforts to
22 conduct the laboratory experiments presented here.

1 **References**

2 **References**

3 Arega, F., Sanders, B.F., 2004. Dispersion model for tidal wetlands. *J. Hy-*
4 *draul. Eng.* 130(8), 739–754.

5 Bates, P.D., Horritt, M.S., Fewtrell, T.J., 2010. A simple inertial formulation
6 of the shallow water equations for efficient two-dimensional flood inunda-
7 tion modelling. *J. Hydrol.* 387, 33–45.

8 Bates, P.D., 2012. Integrating remote sensing data with flood inundation
9 models: how far have we got? *Hydrol. Process.* 26, 2515–2521.

10 Bear, J., 1988 *Dynamics of Fluids in Porous Media*, Second Edition (of the
11 1972 book) Dover Publ., New York, 761p.

12 Begnudelli, L., Sanders, B.F., Bradford, S.F., 2008. An adaptive Godunov-
13 based model for flood simulation. *J. Hydraul. Eng.* 134(6), 714–725.

14 Cea, L., Vázquez-Cendón, M.E., 2010. Unstructured finite volume discretiza-
15 tion of two-dimensional depth-averaged shallow water equations with
16 porosity. *Int. J. Num. Meth. Fluid.* 63, 903–930.

17 Chen, A., Evans, B., Djordjević, S., Savić, D.A., 2012. A coarse-grid ap-
18 proach to represent building blockage effects in 2D urban flood modelling,
19 *J. Hydrol.* 426–427, 1–16.

20 Defina, A., 2000. Two-dimensional shallow flow equations for partially dry
21 areas. *Water Resour. Res.* 36(11), 3251–3264.

- 1 Guinot, V., 2012. Multiple porosity shallow water models for macroscopic
2 modelling of urban floods. *Adv. Water Resour.* 37, 40–72.
- 3 Haaland, S.E., 1983. Simple and explicit formulas for the friction factor in
4 turbulent pipe flow. *J. Fluids Eng.* 105(1), 89–90.
- 5 Kim, B., Sanders, B.F., Schubert, J.E., Famiglietti, J.S., 2014. Mesh type
6 tradeoffs in 2D hydrodynamic modeling of flooding with a Godunov-based
7 flow solver. *Adv. Water Resour.* 68, 42–61.
- 8 McMillan, H.K., Brasington, J., 2007. Reduced complexity strategies for
9 modelling urban floodplain inundation. *Geomorphology* 90, 226–243.
- 10 Munson, B.R., Young, D.F., Okiishi, T.H., 2006. *Fundamentals of fluid me-*
11 *chanics*, 5th ed., John Wiley & Sons, 769p.
- 12 Nepf, H.M., 1999. Drag, turbulence and diffusion in flow through emergent
13 vegetation. *Water Resour. Res.* 35(2), 479–489.
- 14 Sampson, C.C., Fewtrell, T.J., Duncan, A., Shaad, K., Horritt, M.S., Bates,
15 PD., 2012. Use of terrestrial laser scanning data to derive decimetric res-
16 olution urban inundation models. *Adv. Water Resour.* 41, 1–17.
- 17 Sanders, B.F., 2008. Integration of a shallow-water model with a local time
18 step. *J. Hydraul. Res.* 46(8), 466–475.
- 19 Sanders, B.F., Schubert, J.E., Gallegos, H.A., 2008. Integral formulation of
20 shallow-water equations with anisotropic porosity for urban flood model-
21 ing. *J. Hydrol.* 362, 19–38.

- 1 Schubert, J.E., Sanders, B.F., 2012. Building treatments for urban flood
2 inundation models and implications for predictive skill and modeling effi-
3 ciency. *Adv. Water Resour.* 41, 49–64.
- 4 Soares-Frazão, S., Lhomme, J., Guinot, V., Zech, Y., 2008. Two-dimensional
5 shallow-water model with porosity for urban flood modelling. *J. Hydraul.*
6 *Res.* 46(1), 45–64.
- 7 Soares-Frazão, S., Zech, Y., 2008. Dam-break flow through an idealized city.
8 *J. Hydraul. Res.* 46(5), 648–658.
- 9 Stelling, G.S., 2012. Quadtree flood simulations with sub-grid digital eleva-
10 tion models. *Proc. Inst. Civ. Eng.-Water Manag.* 165(10), 567–580.
- 11 Testa, G., Zuccala, D., Alcrudo, F., Mulet, J., Soares-Frazão, S., 2007. Flash
12 flood flow experiment in a simplified urban district. *J. Hydraul. Res.* 45(Ex-
13 tra Issue), 37–44.
- 14 Yoon, K., 2007. Experimental study on flood inundation considering urban
15 characteristics (FFC06-05). Urban Flood Disaster Management Research
16 Center, Seoul.
- 17 Yu, D., Lane, S.N., 2005. Urban fluvial flood modelling using a two dimen-
18 sional diffusion-wave treatment, part 2: development of a sub-grid-scale
19 treatment. *Hydrol. Process.* 20(7), 1567–1583.

1 Captions of Figures

- 2 • Fig. 1. Experiment set-up of Yoon (Yoon, 2007): (a) Plan view, (b)
3 Side view, and (c) Close-up of greyed section in Fig. 1(a); and (d) Cell-
4 based porosity ϕ exhibits heterogeneity depending on control volume
5 placement, a vs. b , and edge-based porosities ψ exhibit heterogeneity
6 and anisotropy depending on the chosen transect.

- 7 • Fig. 2. Computational mesh for (a) CSW and CSW-P, (b) PSW-A,
8 PSW-I-2A and PSW-I-2A, and (c) PSW-I-1A and PSW-I-1B.

- 9 • Fig. 3. Contours of water depth 50 s after dam-break on CSW-S with
10 (a) 0.05 m and (b) 0.025 m resolution. Vectors indicate velocity direc-
11 tion.

- 12 • Fig. 4. Flood depth sensitivity to roughness height (k_s) on CSW.

- 13 • Fig. 5. Comparison of predicted flood depth and measurement for
14 $h_0=0.30$ m.

- 15 • Fig. 6. Comparison of predicted flood depth and measurement for
16 $h_0=0.45$ m.

- 17 • Fig. 7. Comparison of predicted flood velocity for $h_0=0.30$ m.

- 18 • Fig. 8. Comparison of predicted flood velocity for $h_0=0.45$ m.

- 19 • Fig. 9. Contours of water depth 50 s after dam-break on (a) CSW-
20 P, (b) PSW-A, (c) PSW-I-1A, (d) PSW-I-1B, (e) PSW-I-2A and (f)
21 PSW-I-2B. Vectors indicate velocity direction.

- 1 • Fig. 10. Profile of flood depth after dam-break for $h_0=0.30$ m at B-B'in
- 2 Fig. 1(c).

1 **Captions of Tables**

- 2 • Table 1. Shallow-water model formulations and corresponding meshes
3 shown in Fig. 2.
- 4 • Table 2. L_1 norms of flood depth for calibration of roughness height
5 (k_s) on CSW (unit: cm).
- 6 • Table 3. L_1 norms of flood depth for calibration of drag coefficient (c_D^o)
7 on PSW-A and PSW-I.
- 8 • Table 4. Model parameters and run time.
- 9 • Table 5. L_1 norms of flood depth and velocity based on calibration and
10 reference solution.

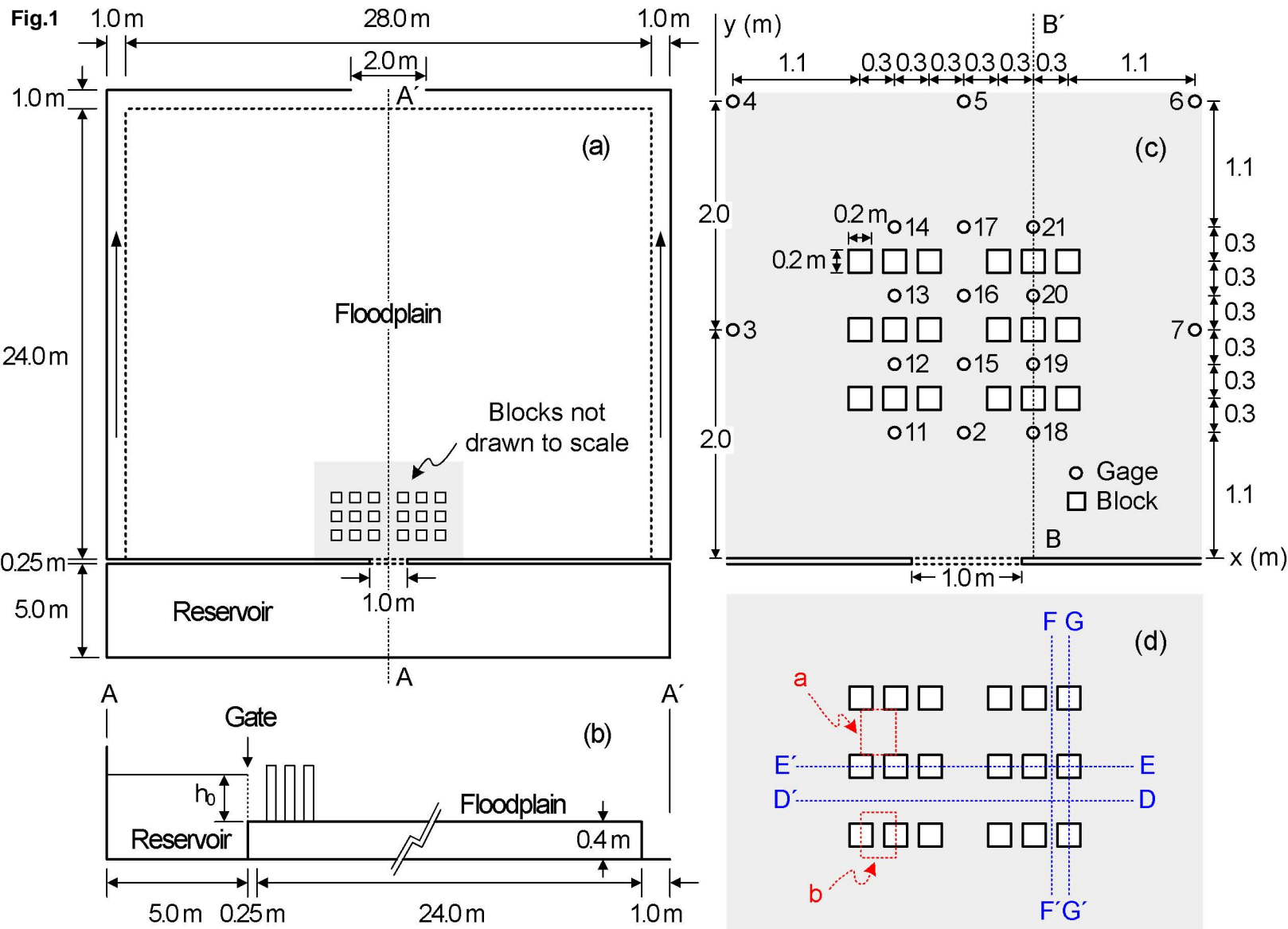


Fig. 1. Experiment set-up of KICT (Yoon, 2007): (a) Plan view, (b) Side view, and (c) Close-up of greyed section in Fig. (a); and (d) Cell-based porosity ϕ exhibits heterogeneity depending on control volume placement, a vs. b , and edge-based porosities ψ exhibit heterogeneity and anisotropy depending on the chosen transect.

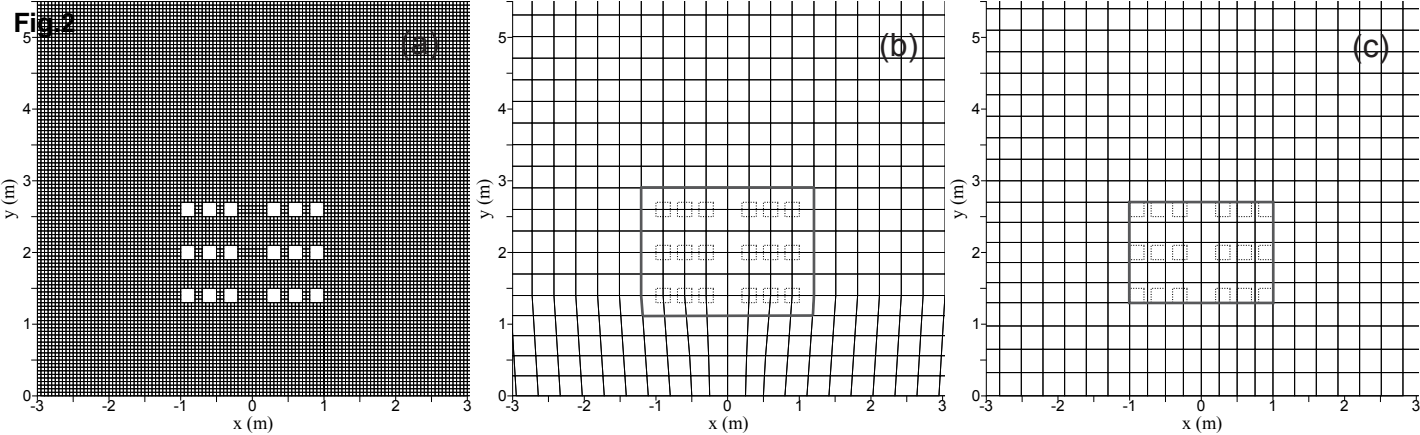


Fig. 3. Computational mesh for (a) CSW and CSW-P, (b) PSW-A, PSW-I-2A and PSW-I-2B, and (c) PSW-I-1A and PSW-I-1B.

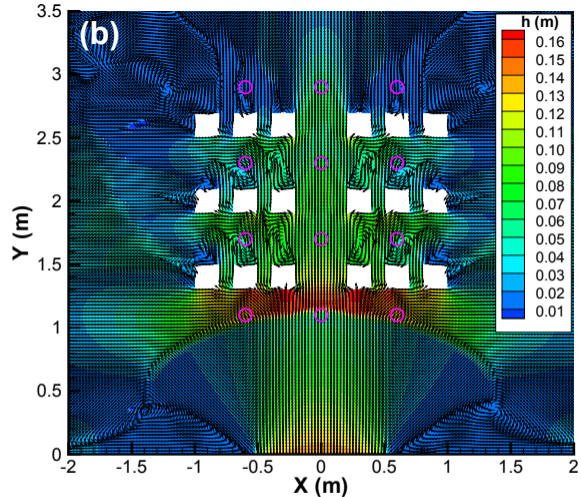
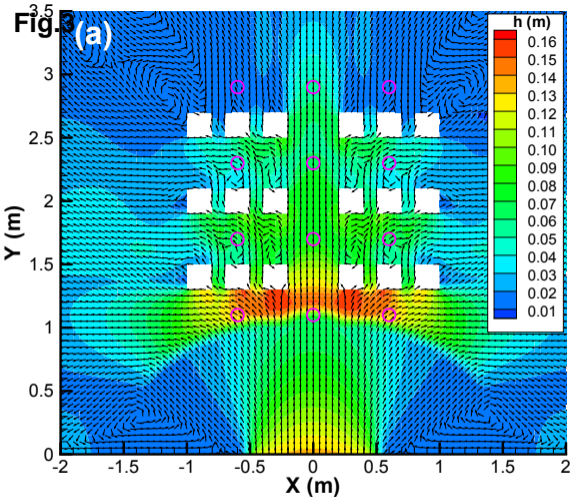


Fig. 3. Contours of water depth 50 s after dam-break on CSW with (a) 0.05 m and (b) 0.025 m resolution. Vectors indicate velocity direction.

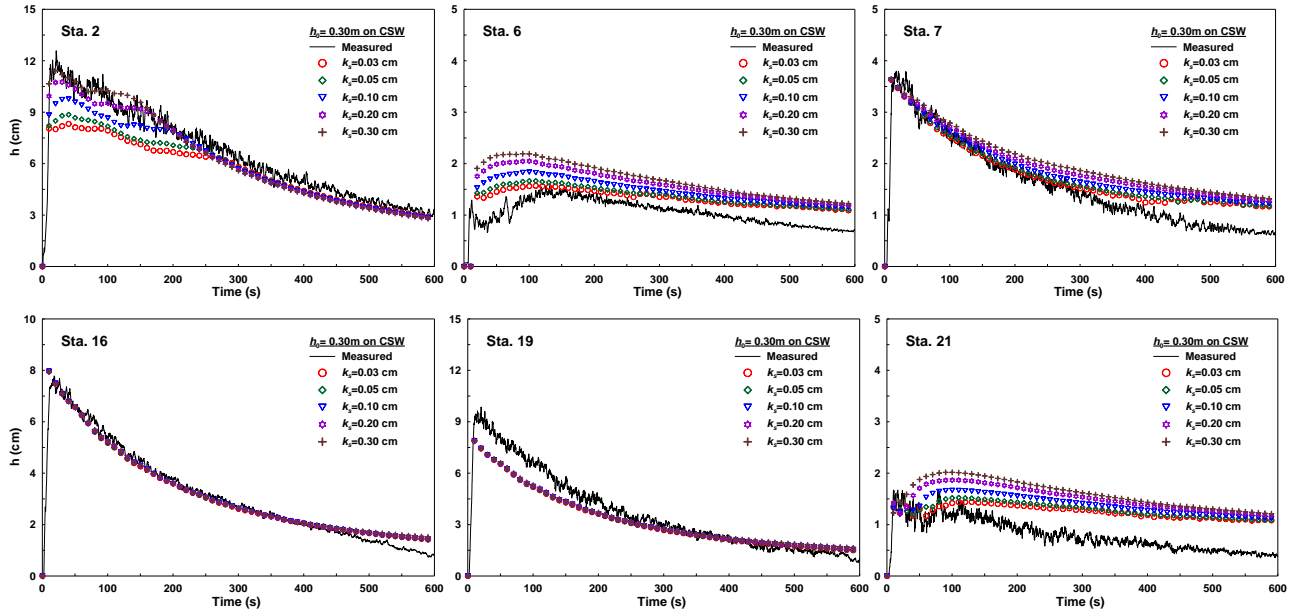


Fig. 4. Flood depth sensitivity to roughness height (k_s) on CSW.

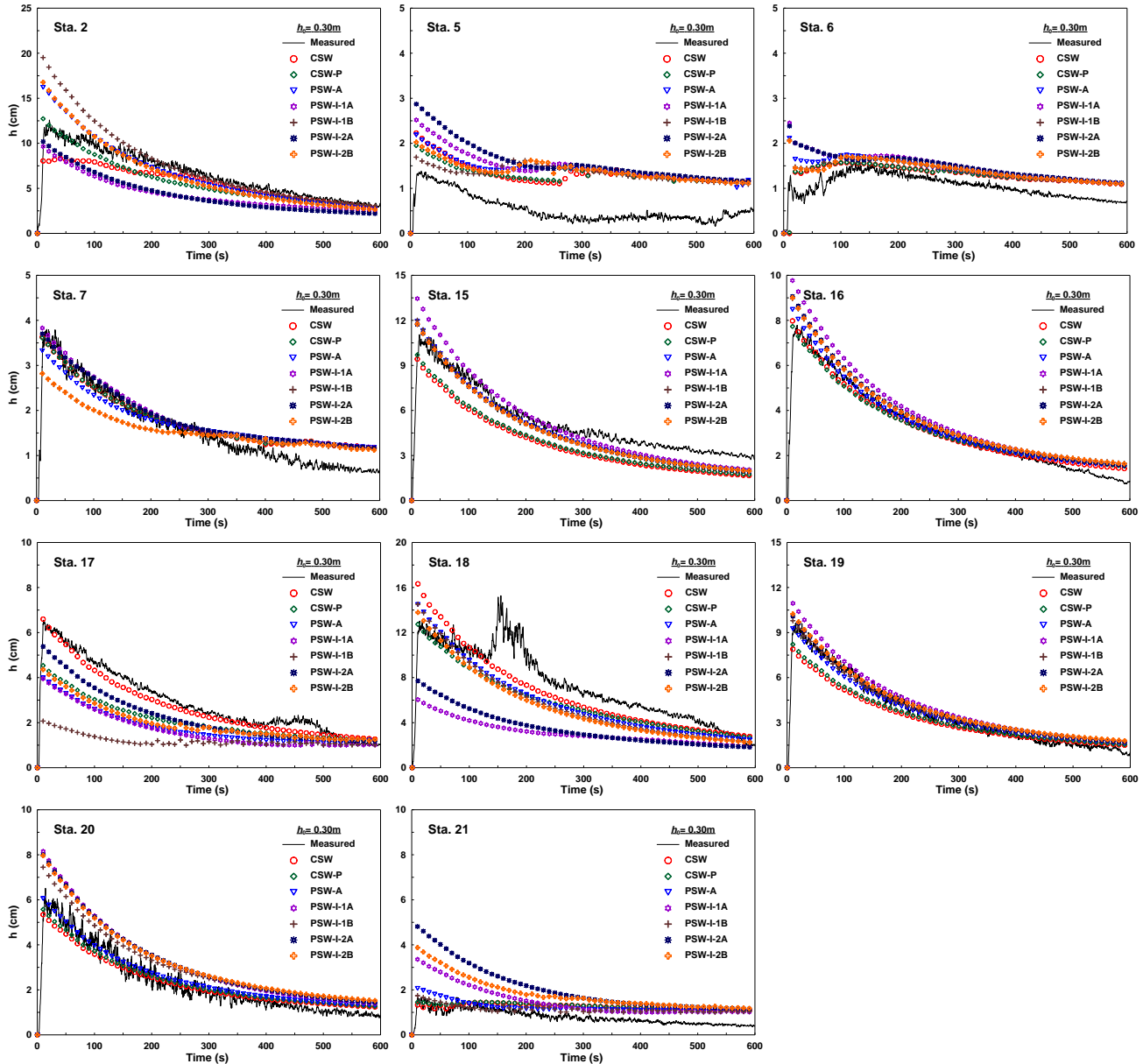


Fig. 5. Comparison of predicted flood depth and measurement for $h_0=0.30$ m.

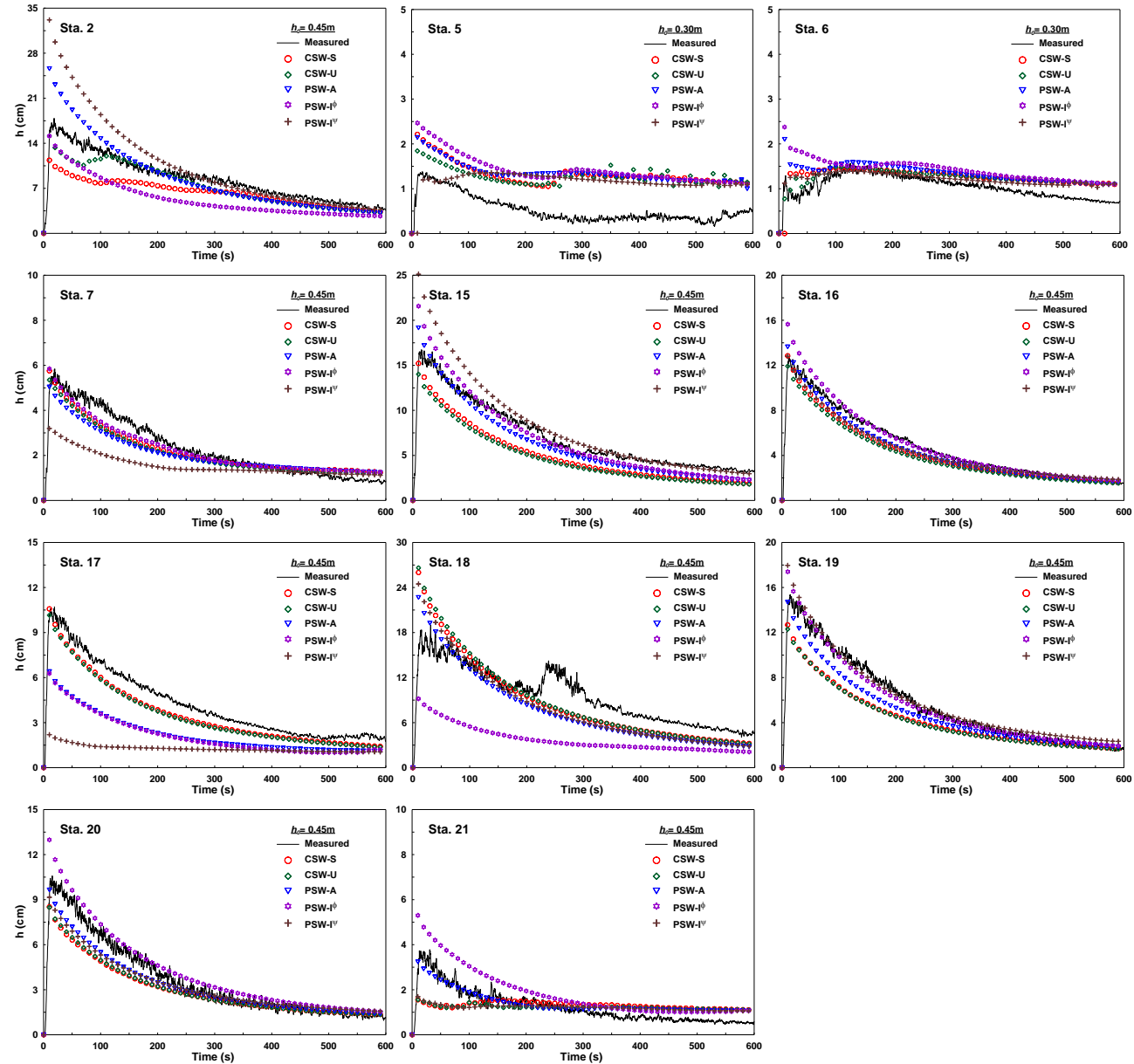


Fig. 6. Comparison of predicted flood depth and measurement for $h_0=0.45$ m.

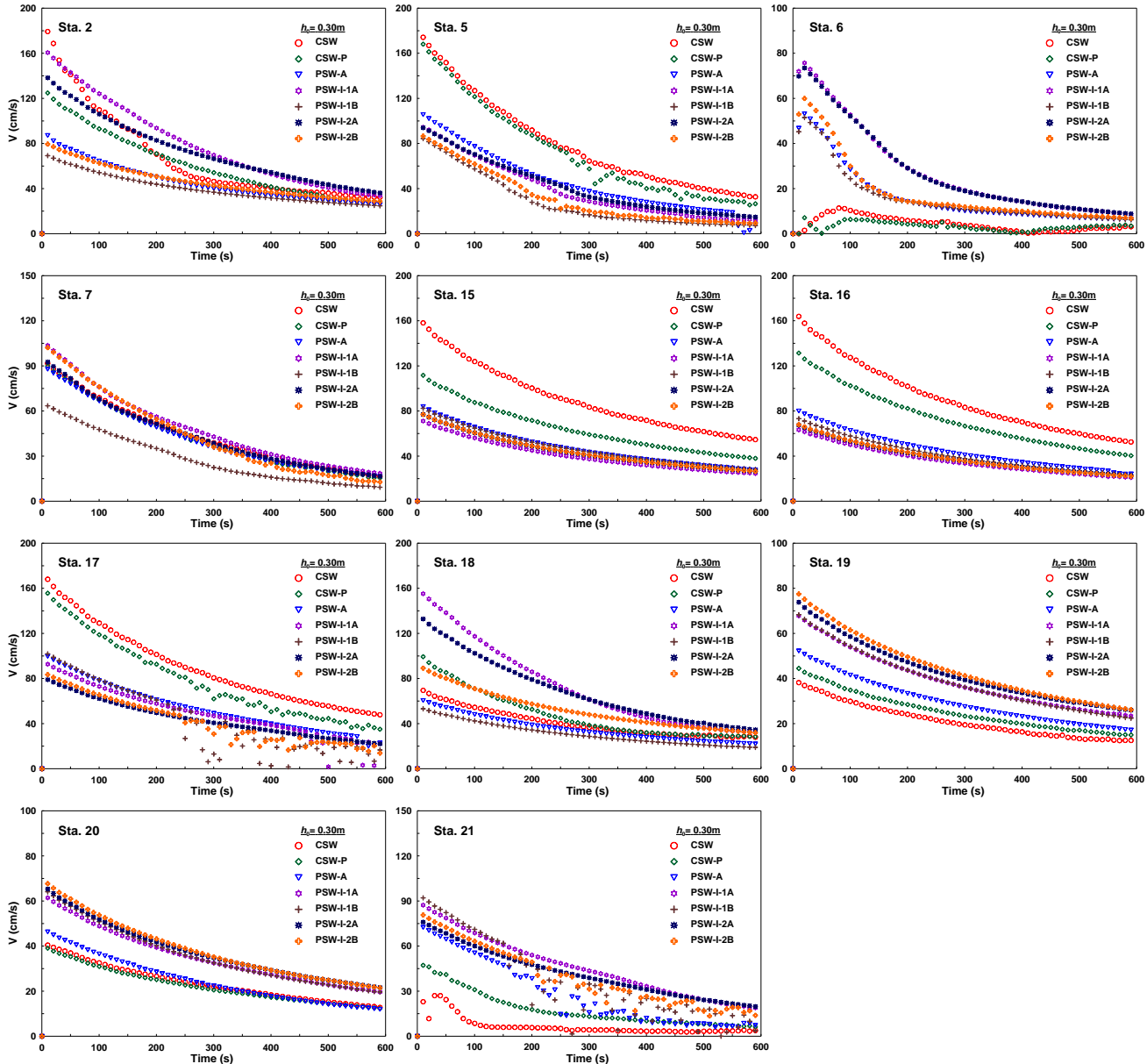


Fig. 7. Comparison of predicted velocity for $h_0=0.30$ m.

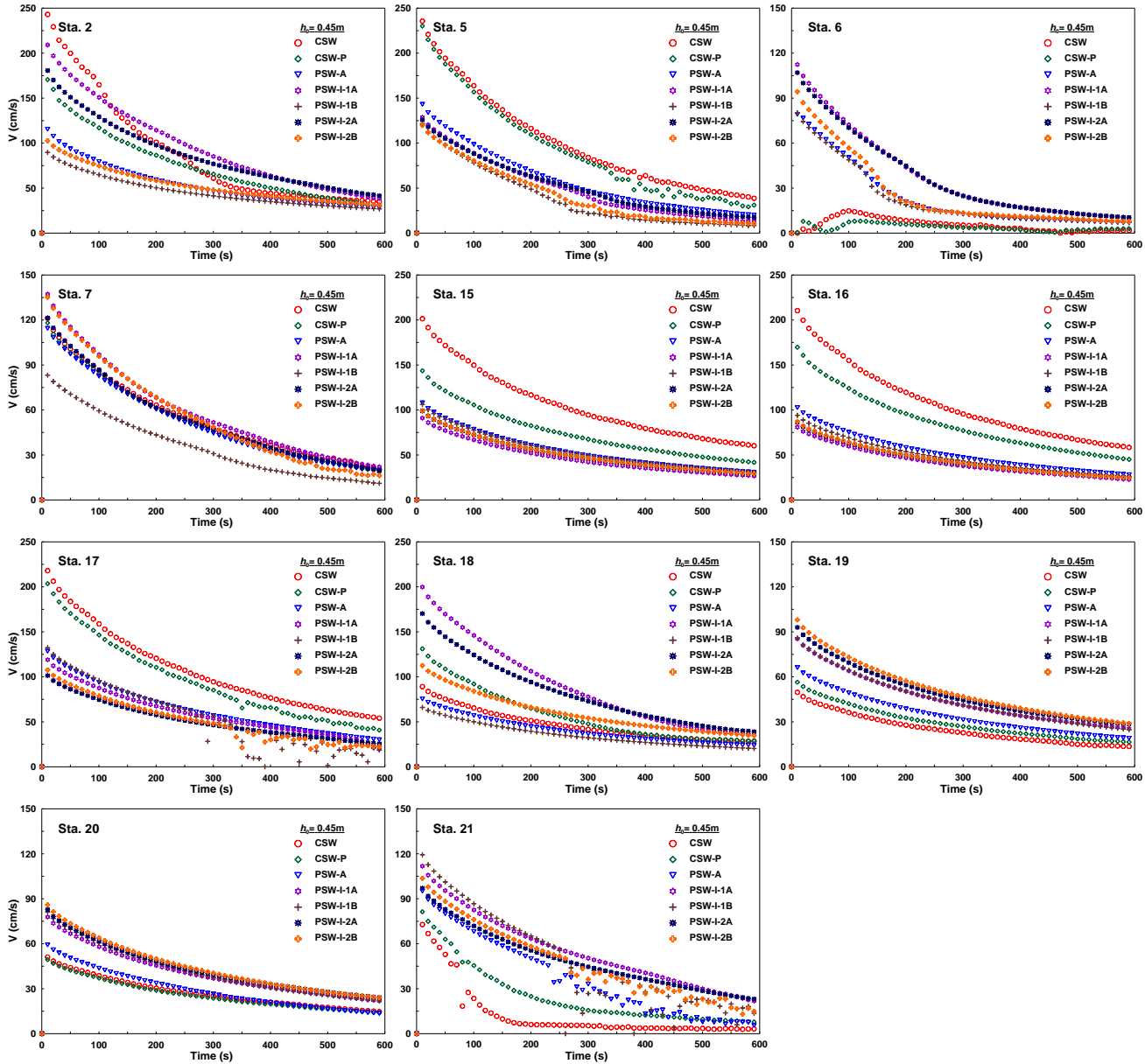


Fig. 8. Comparison of predicted velocity for $h_0=0.45\text{m}$.

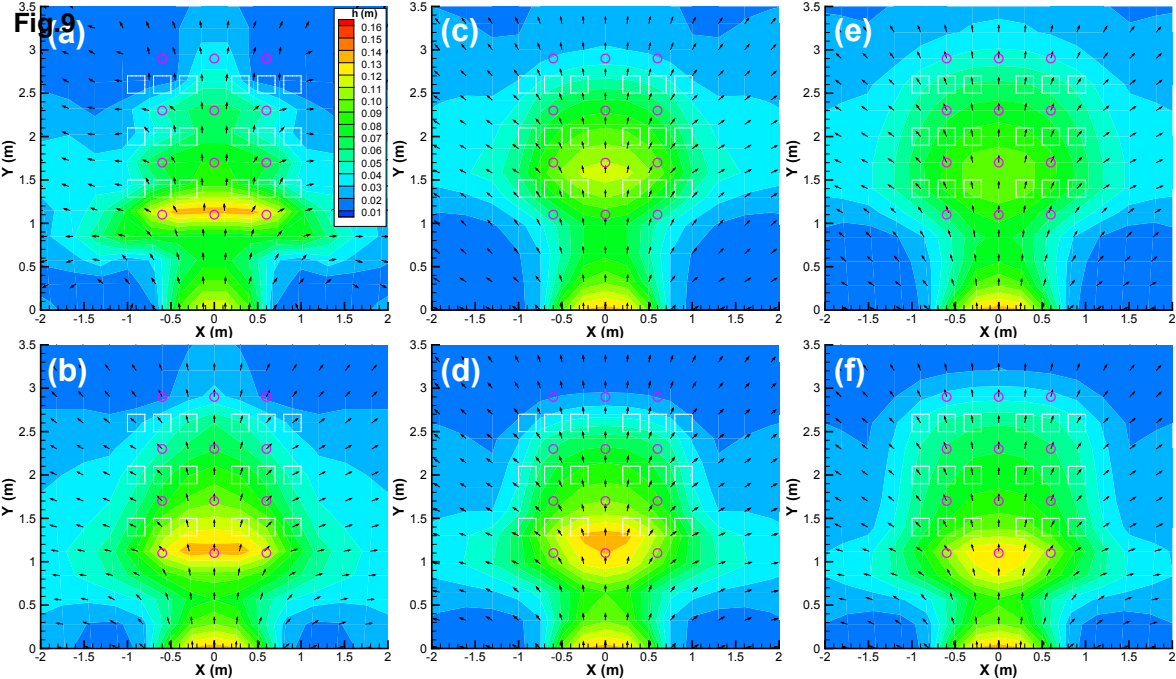


Fig. 10. Contours of water depth 50 s after dam-break on (a) CSW-P, (b) PSW-A, (c) PSW-I-1A, (d) PSW-I-1B, (e) PSW-I-2A and (f) PSW-I-2B. Vectors indicate velocity direction.

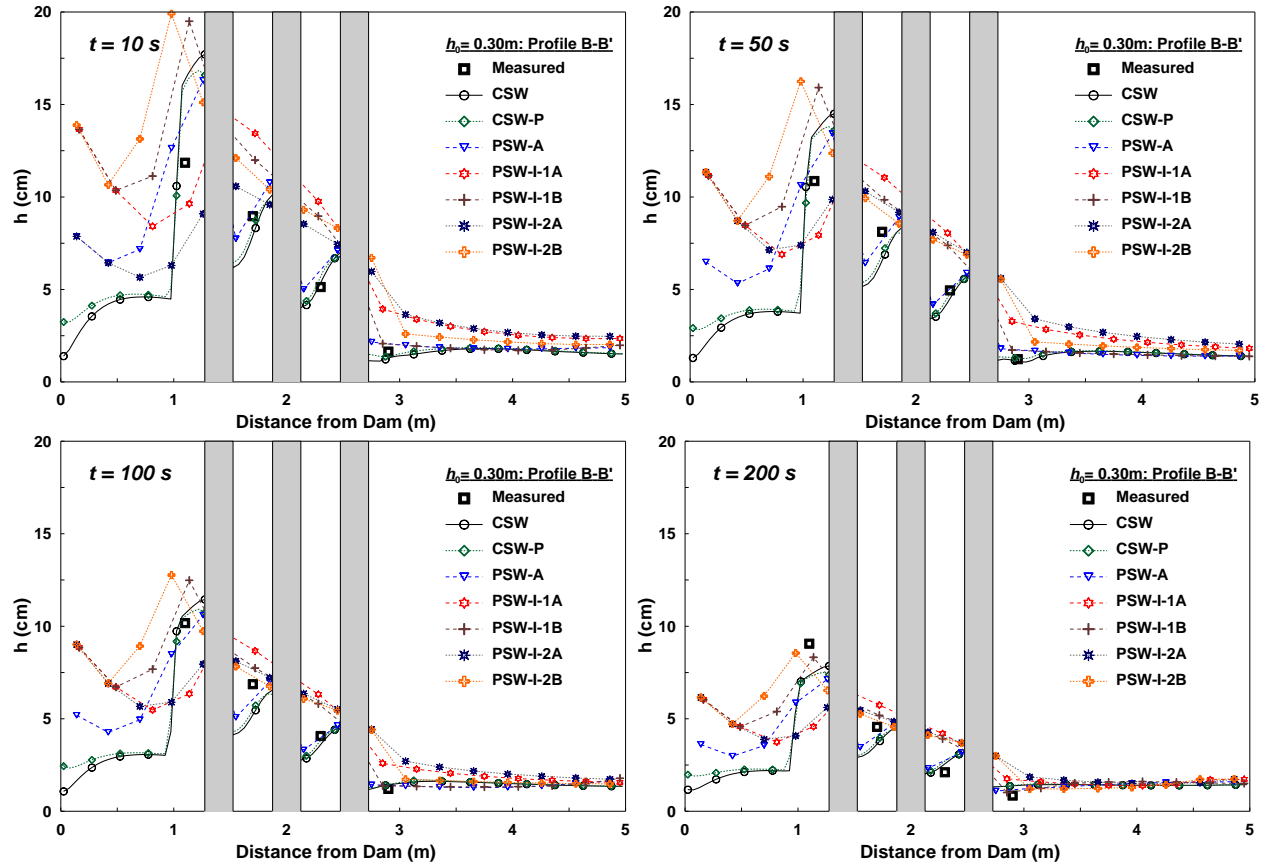


Fig. 9. Profile of flood depth after dam-break for $h_0=0.30$ m at B-B' in Fig. 1(c).

Table 1. Shallow-water model formulations and corresponding meshes shown in Fig. 2

Case	Description	Mesh in Fig. 2	Num. of nodes	Num. of cells	Resolution (m)		
					Avg.	Max.	Min.
CSW	Classical shallow-water	(a)	330464	328612	0.05	0.05	0.05
CSW-P	Pore-scale average of CSW	(a)	330464	328612	0.05	0.05	0.05
PSW-A	Anisotropic porosity model	(b)	9216	8932	0.30	0.33	0.25
PSW-I-1A	Isotropic porosity model ($\phi = \psi = 0.74$)	(c)	9412	9124	0.30	0.33	0.25
PSW-I-1B	Isotropic porosity model ($\phi = \psi = 0.40$)	(c)	9412	9124	0.30	0.33	0.25
PSW-I-2A	Isotropic porosity model ($\phi = \psi = 0.83$)	(b)	9216	8932	0.30	0.33	0.25
PSW-I-2B	Isotropic porosity model ($\phi = \psi = 0.50$)	(b)	9216	8932	0.30	0.33	0.25

Table 2. L_1 norms of flood depth for calibration of roughness height (k_s) on CSW (unit: cm).

Case	k_s (cm)	Gages inside block zone									Gages outside block zone				Entire Avg.
		2	11&18	12&19	13&20	14&21	15	16	17	Avg.	3&7	4&6	5	Avg.	
CSW	0.03	1.08	1.22	0.66	0.44	0.58	1.49	0.23	0.29	0.75	0.33	0.39	0.81	0.51	0.63
	0.05	0.94	1.23	0.66	0.44	0.62	1.49	0.23	0.29	0.74	0.35	0.44	0.82	0.54	0.64
	0.10	0.71	1.24	0.66	0.44	0.70	1.48	0.23	0.29	0.72	0.40	0.53	0.89	0.61	0.66
	0.20	0.56	1.25	0.66	0.45	0.83	1.46	0.23	0.30	0.72	0.49	0.66	1.03	0.72	0.72
	0.30	0.57	1.26	0.67	0.46	0.91	1.44	0.23	0.30	0.73	0.56	0.74	1.12	0.81	0.77

Table 3. L_1 norms of flood depth and velocity for calibration of drag coefficient (c_D^o) on PSW-A and PSW-I.

Case	L_1 of flood depth (unit: cm)					L_1 of flood depth (unit: cm)					L_1 of flood velocity (unit: cm/s)				
	Calib1: Ref.-Measured h					Calib2: Ref.-Predicted h on CSW-P					Calib3: Ref.-Predicted V on CSW-P				
	$c_D^o=1.0$	1.5	2.0	2.5	3.0	$c_D^o=1.0$	1.5	2.0	2.5	3.0	$c_D^o=1.0$	1.5	2.0	2.5	3.0
PSW-A	0.705	0.681	0.669	0.663	0.660	0.165	0.186	0.21	0.231	0.248	10.958	11.816	12.513	13.111	13.695
PSW-I-1A	1.068	1.021	1.015	1.012	1.003	0.507	0.545	0.578	0.592	0.590	21.730	21.893	22.132	22.136	21.960
PSW-I-1B	0.751	0.732	0.726	0.728	0.732	0.337	0.387	0.422	0.446	0.464	21.581	21.812	21.956	22.123	22.171
PSW-I-2A	1.152	1.088	1.04	1.003	0.974	0.601	0.529	0.533	0.543	0.533	22.084	21.05	20.798	20.505	20.142
PSW-I-2B	0.815	0.78	0.761	0.752	0.749	0.278	0.284	0.317	0.341	0.360	20.532	20.343	20.204	20.152	20.122

Table 4. Model parameters and run time.

Case	k_s (cm)	c_D^o			ϕ	ψ	a_f (m ⁻¹)	Max. $Cr.$	$h_0 = 0.30$ m		$h_0 = 0.45$ m	
		Calib1	Calib2	Calib3					Δt (s)	Runtime (s)	Δt (s)	Runtime (s)
CSW	0.03	-	-	-	-	-	-	0.6	0.0079	5699	0.0062	7264
CSW-P	0.03	-	-	-	-	-	-	0.6	0.0079	5699	0.0062	7264
PSW-A	0.03	3.0	1.0	1.0	0.76~0.89	0.33~0.67	1.09~2.38	0.6	0.0565	9.34	0.0460	11.34
PSW-I-1A	0.03	3.0	1.0	1.0	0.74	0.74	1.29	0.6	0.0563	9.45	0.0460	11.58
PSW-I-1B	0.03	2.0	1.0	1.0	0.40	0.40	1.29	0.6	0.0563	9.45	0.0460	11.53
PSW-I-2A	0.03	3.0	1.5	3.0	0.83	0.83	0.83	0.6	0.0564	9.38	0.0460	11.28
PSW-I-2B	0.03	3.0	1.0	3.0	0.50	0.50	0.83	0.6	0.0564	9.39	0.0460	11.25

Table 5. L_1 norms of flood depth and velocity based on calibration and reference solution.

h_0 (m)	Case	L_1 of flood depth (unit: cm)			L_1 of flood depth (unit: cm)			L_1 of flood velocity (unit: cm/s)		
		Ref. - Measured h			Ref. - Predicted h on CSW-P			Ref. - Predicted V on CSW-P		
		Calib1	Calib2	Calib3	Calib1	Calib2	Calib3	Calib1	Calib2	Calib3
0.30	CSW	0.63	0.63	0.63	0.18	0.18	0.18	7.45	7.45	7.45
	CSW-P	0.66	0.66	0.66	-	-	-	-	-	-
	PSW-A	0.66	0.70	0.70	0.25	0.17	0.17	13.70	10.96	10.96
	PSW-I-1A	1.00	1.07	1.07	0.59	0.51	0.51	21.96	21.73	21.73
	PSW-I-1B	0.73	0.75	0.75	0.42	0.34	0.34	21.93	21.58	21.58
	PSW-I-2A	0.97	1.09	0.97	0.53	0.53	0.53	20.14	21.05	20.14
	PSW-I-2B	0.75	0.81	0.75	0.36	0.28	0.36	20.12	20.53	20.12
0.45	CSW	0.89	0.89	0.89	0.30	0.30	0.30	9.12	9.12	9.12
	CSW-P	0.89	0.89	0.89	-	-	-	-	-	-
	PSW-A	0.87	0.91	0.91	0.36	0.22	0.22	17.90	14.35	14.35
	PSW-I-1A	1.15	1.39	1.39	0.81	0.71	0.71	27.46	28.16	28.16
	PSW-I-1B	0.95	1.05	1.05	0.62	0.50	0.50	27.29	27.27	27.27
	PSW-I-2A	1.15	1.40	1.15	0.73	0.74	0.73	25.04	26.32	25.04
	PSW-I-2B	0.91	1.12	0.91	0.52	0.39	0.52	25.35	25.78	25.35